The magnetic local time distribution of energetic electrons in the radiation belt region

Hayley J. Allison[1,2] (iD), **Richard B. Horne**[1] (iD), **Sarah A. Glauert**[1], and **Giulio Del Zanna**[2]

[1]British Antarctic Survey, Natural Environment Research Council, Cambridge, UK, [2]Department of Applied Mathematics and Theoretical Physics, University of Cambridge, Cambridge, UK

Correspondence to:
H. J. Allison,
haylis@bas.ac.uk

Abstract Using 14 years of electron flux data from the National Oceanic and Atmospheric Administration Polar Operational Environmental Satellites, a statistical study of the magnetic local time (MLT) distribution of the electron population is performed across a range of activity levels, defined by AE, AE^*, Kp, solar wind velocity (V_{sw}), and $V_{sw}B_z$. Three electron energies (>30, >100, and >300 keV) are considered. Dawn-dusk flux asymmetries larger than order of magnitude were observed for >30 and >100 keV electrons. For >300 keV electrons, dawn-dusk asymmetries were primarily due to a decrease in the average duskside flux beyond $L^* \sim 4.5$ that arose with increasing activity. For the >30 keV population, substorm injections enhance the dawnside flux, which may not reach the duskside as the electrons can be on open drift paths and lost to the magnetopause. The asymmetries in the >300 keV population are attributed to the combination of magnetopause shadowing and >300 keV electron injections by large electric fields. We suggest that 3-D radiation belt models could set the minimum energy boundary (E_{min}) to 30 keV or above at $L^* \sim 6$ during periods of low activity. However, for more moderate conditions, E_{min} should be larger than 100 keV and, for very extreme activities, $\sim$300 keV. Our observations show the extent that in situ electron flux readings may vary during active periods due to the MLT of the satellite and highlight the importance of 4-D radiation belt models to fully understand radiation belt processes.

1. Introduction

Electrons in the energy range of a few keVs to a few hundred keVs are transported into the inner magnetosphere from the nightside plasma sheet by substorm injections [*Arnoldy and Chan*, 1969; *Cayton et al.*, 1989; *Birn et al.*, 1998]. Subsequent acceleration of these injected electrons is thought to form the >1 MeV population of the radiation belts [*Horne and Thorne*, 2003; *Horne et al.*, 2005; *Boyd et al.*, 2016]. Potential mechanisms for such acceleration include inward radial transport [*O'Brien et al.*, 2001; *Mann et al.*, 2004] and local acceleration via wave-particle interactions [*Horne et al.*, 2005, 2007; *Thorne*, 2010; *Reeves et al.*, 2013]. Recent studies focused on the latter have highlighted the importance of chorus waves for local acceleration [*Thorne et al.*, 2013; *Li et al.*, 2014]. This has lead to the proposition of a source-seed mechanism, whereby injected electrons below a few tens of keV (the source population) fuel chorus waves that can then act to accelerate higher-energy electrons (30–300 keV, known as the seed population) up to relativistic energies [*Thorne et al.*, 2013; *Jaynes et al.*, 2015]. Here the seed population is also injected by substorms. Both the source and seed population are critical to this process, and if either is absent then acceleration is unlikely to occur [*Jaynes et al.*, 2015]. The implication is that understanding the energy-dependent dynamics of injected electrons appears to be crucial to ultimately understand the occurrence of the MeV energy population.

Since electron drift motion around the Earth is energy dependent, the electron distribution subsequent to substorm injection is likely to exhibit a variation in magnetic local time (MLT) that depends on energy. For relativistic electrons (typically ~1 MeV), magnetic drifts dominate, resulting in closed drift paths throughout most of the radiation belt region. At lower electron energies, the energy-dependent magnetic drifts are less significant and convective motion can become influential for parts of the outer radiation belt and beyond. With increasing convective electric field strength, this region can penetrate to lower L shells. However, even for electrons of a few eV, the convection electric field cannot dominate the drift motion below the Alfvén layer due to the presence of the corotation electric field, causing electrons to circulate around the Earth. As the convective drift is in a sunward direction, the combination of this motion and magnetic drifts results in open drift paths that transit the dawnside of the Earth before impinging the magnetopause

[*Kavanagh et al.*, 1968; *Chen and Schulz*, 2001]. Statistical studies of the global distribution of precipitating ≤12 keV electrons [*Hardy et al.*, 1985] and trapped suprathermal (0.1–16.5 keV) electrons [*Li et al.*, 2010; *Bortnik et al.*, 2007; *Meredith et al.*, 2004] have demonstrated an enhanced electron flux in the dawn sector during periods of high activity. For higher-energy electrons, such statistical studies are less extensive. *Meredith et al.* [2016] presented the global distribution of seed population electrons observed for $AE > 300$ nT, while *Thorne et al.* [2007] used more than a year of data from multiple passes of a single satellite to construct the statistical distribution of 153 keV and 340 keV electron flux for three levels of activity, defined by AE^*. In both studies an MLT variation was observed for electrons with energies exceeding 100 keV, but this was unclear for energies greater than 300 keV.

Present 3-D global models of the radiation belts use a drift-averaged approximation, essentially assuming that the electron flux and diffusion coefficients can be averaged over a drift path and the calculation performed using these drift-averaged values [e.g., *Varotsou et al.*, 2005; *Albert et al.*, 2009; *Shprits et al.*, 2011; *Glauert et al.*, 2014a; *Tu et al.*, 2014]. When the electron flux is mostly uniform in MLT, the drift-average approximation is a useful simplification to the calculation, removing the MLT dimension. While wave-particle interactions exhibit an MLT dependence [*Meredith et al.*, 2004, 2012; *Sigsbee et al.*, 2010; *Kersten et al.*, 2014], the timescale of the azimuthal drift for the MeV energy electrons is short in comparison with the timescale for acceleration or scattering. The electrons rapidly move through regions where wave-particle interactions occur and then, as they are on closed drift paths, shortly return. The net result is that changes in the electron flux at MeV energies are mostly uniform in MLT. However, lower energy electrons, which drift more slowly and may potentially be on open drift paths, are more likely to exhibit a higher flux in regions where chorus waves are typically observed [*Horne et al.*, 2013] and a lower flux in a loss region. To account for this, 3-D radiation belt models can attempt to exclude electron energies which may demonstrate significant MLT variations when selecting the minimum energy of the calculation region. Currently, various global models use a range of values for the lower bound of the energy. The Versatile Electron Radiation Belt-3D typically sets the minimum energy at 10 keV [*Shprits et al.*, 2011; *Subbotin and Shprits*, 2009; *Kim and Shprits*, 2013], the Salammbô model at 10 keV [*Varotsou et al.*, 2005, 2008], the British Antarctic Survey Radiation Belt Model (BAS-RBM) at 153 keV [*Glauert et al.*, 2014a], *Ma et al.* [2015] at 180 keV, and *Albert et al.* [2009] at 200 keV. To the knowledge of the authors there has not been any systematic study to determine the nonuniformity of the electron flux with MLT at these energies.

The purpose of this paper is to investigate the >30, >100, and >300 keV electron flux observed by the Polar Observational Environmental Satellites (POES) to quantify at what energies notable MLT variations occur, and hence the minimum electron energy which may be included in 3-D radiation belt calculations. The MLT distribution of the electron flux is evaluated at several activity levels to account for changes in the convection electric field with activity [*Kivelson*, 1976] and the occurrence of substorm injections. Such a survey is possible as the POES constellation provides high time resolution multipoint electron flux measurements, covering several MLTs, across a broad range of L shells. Previous work has considered the energy-dependent radial structure of the radiation belts using data from the Van Allen Probes satellites [*Reeves et al.*, 2016]. Here we study a wider L shell range than possible with the Van Allen Probes and additionally consider the energy-dependent MLT structure.

2. Instrumentation and Data Set

In this study 14 years of data from the POES satellites were used, spanning from 1 January 2000 to 31 December 2013. As shown in Figure 1, this date range covers just over one solar cycle, including the declining phase of cycle 23 along with the rising phase of 24 so that the electron flux for a wide range of geomagnetic activity is included in our analysis.

2.1. NOAA POES Satellites

The POES constellation consists of low-altitude polar-orbiting satellites that each transit the Earth approximately 14 times a day, operating at an altitude of around 820 km. Due to the ~98.5° inclination polar orbit, an L^* range spanning from $L^* < 1.3$ to $L^* > 9$ can be crossed during a pass, dependent on activity. As the orbital period of POES is ~100 min and the data sampling rate is 2 s, the high inclination orbit provides a cross section through the radiation belts every quarter period, with a resolution of ~25 min. Each POES satellite is Sun-synchronous and operates over a limited range of MLTs. During the time period examined, there are
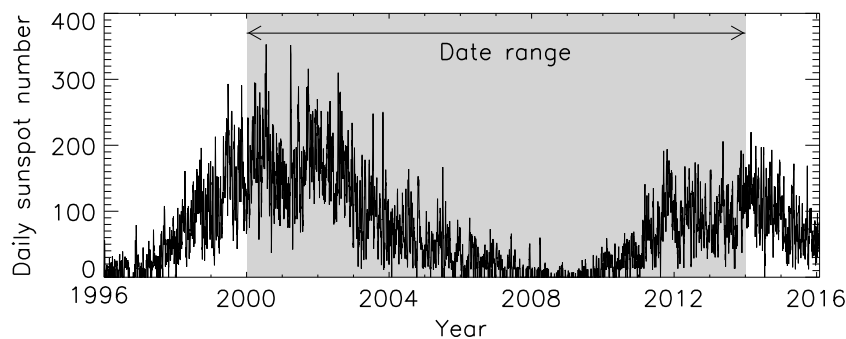
**Figure 1.** Date range investigated in relation to the solar cycle.

up to six POES satellites operational at any time, providing multipoint MLT observations. Coupled with the L^* range covered during an orbit, the POES constellation provides very rapid and complete observations of the radiation belt region.

On board the POES satellites NOAA15, NOAA16, NOAA17, NOAA18, NOAA19, and METOP02 is the Space Environment Monitor, which contains the Medium Energy Proton and Electron Detector (MEPED). The MEPED instruments on board each satellite were all built at the same time and cross calibrated before being deployed. Furthermore, the instruments undergo a weekly in-flight calibration procedure, as detailed in *Evans and Greer* [2004]. No further cross calibration has been applied to the data. MEPED measures electron flux data in three energy channels, >30, >100, and >300 keV [*Evans and Greer*, 2004]. The upper limit of each energy range is 2.5 MeV; however, as electron energy distribution functions show strong negative gradients with increasing energy [*Cayton et al.*, 1989; *Sergeev et al.*, 1992], the flux measurements are dominated by electrons with energies just above the lower cutoff. The MEPED instrument has two solid-state detector telescopes, T0 and T90, mounted such that each measures electrons at different pitch angles. T0 is aligned so that the field-of-view center axis is rotated 9° from the outward normal to the velocity vector. The other telescope, T90, is orientated perpendicular to T0 so that the center of the field of view is 9° from the direction antiparallel to the spacecraft's velocity. Generally, T90 observes stably trapped electrons or those in the drift or bounce loss cone [*Rodger et al.*, 2010a], while T0 measures precipitating flux, primarily in the bounce loss cone [*Rodger et al.*, 2010b]. At low L^*, this can reverse and T90 observes electrons in the bounce loss cone while T0 can observe trapped flux. A selection procedure has been applied to ensure that only measurements taken outside the drift and bounce loss cone were included in the study. T0 only observes trapped flux for some magnetic longitudes in the equatorial region, relating to $L^* \lesssim 1.5$. T90, on the other hand, observes trapped flux down to $L^* \lesssim 2$ over the South Atlantic Anomaly. For $1.5 < L^* < 2$, neither telescope measures trapped electron flux.

The 2 s resolution electron flux data were used in this study. During solar proton events, contamination of the measured electron flux may occur. To avoid this, periods when the level of >10 MeV protons, measured by the Energetic Particle Sensor of the Geostationary Operational Environmental Satellites (GOES) 10 and GOES 13, exceeded 10 cm^{-2} s^{-1} sr^{-1} were omitted from the study. This is the NOAA Space Weather Prediction Center's definition of a solar proton event and has been adopted by previous authors [e.g., *Lam et al.*, 2010; *Meredith et al.*, 2016]. Additionally, the measured electron flux values were corrected for ring current protons using the bow tie method described by *Lam et al.* [2010].

2.2. Estimates of the Cumulative Distribution Functions of Activity Measures

Activity data spanning the selected date range were used to produce the cumulative distribution functions (CDFs) of AE, AE^*, Kp, solar wind speed (V_{sw}), and $V_{sw}B_z$ (the solar wind speed multiplied by the z component of the interplanetary magnetic field). The AE^* index, first introduced by *Meredith et al.* [2004], is defined as the highest value of the AE index in the preceding 3 h. This helps account for the travel time of injected electrons to transit away from the nightside of the planet. From the CDFs, shown in Figure 2, the activity values corresponding to the 40th, 60th, 80th, 95th, and 98th percentiles were calculated. These values were then used to bound six activity levels for each of the five activity measures and are listed in Table 1. By assigning levels of activity based on probability, statistical consistency was ensured across different parameters. The above percentiles were selected as these adequately captured low to extreme activity, giving a notable change between each level. For $V_{sw}B_z$, the axis has been reversed so that periods of very negative $V_{sw}B_z$ were assigned as high activity.
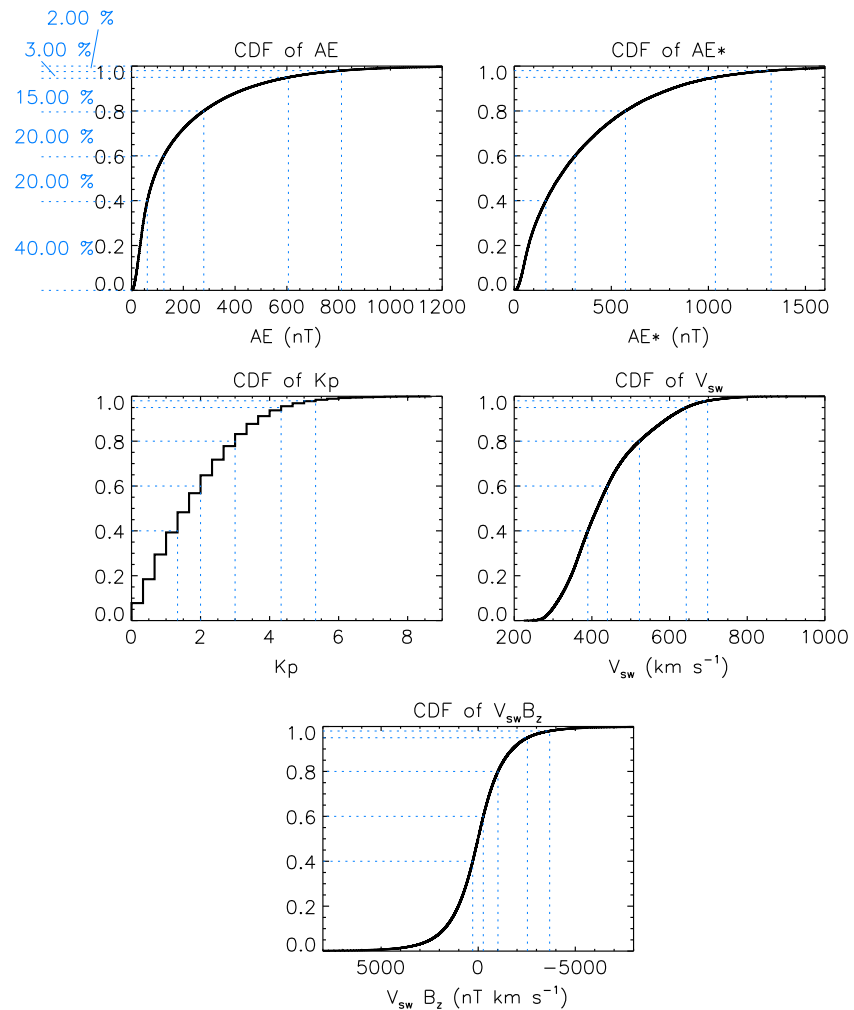
Figure 2. The cumulative distribution functions for AE, $AE*$, Kp, V_{sw}, and $V_{sw}B_z$ activity measures from 1 January 2000 to 31 December 2013. Dotted lines correspond to the 40th, 60th, 80th, 95th, and 98th percentiles chosen to bound the six activity levels. The percentage of activity data contained within each level is marked on the left-hand side of the panel.

The CDFs for AE, $AE*$, and Kp all display a similar shape, skewed toward lower values. In contrast, the shape of the V_{sw} curve indicates that it is distributed about a central speed, with exceedingly low values being a rare occurrence. Interestingly, while speeds above 550 km s^{-1} are sometimes regarded at a fast solar wind speed [*Denton and Borovsky*, 2012], $Kp \sim 3$ or $AE \sim 300$ nT is generally considered only moderate, but all have a similar likelihood of occurrence. The CDF for $V_{sw}B_z$ is almost centered on zero, implying that periods of positive and negative $V_{sw}B_z$ have near equal rates of occurrence.

Table 1. Activity Level Boundaries for AE, $AE*$, Kp, V_{sw}, and $V_{sw}B_z$

	AE (nT)	$AE*$ (nT)	Kp	V_{sw} (km s^{-1})	$V_{sw}B_z$ (nT km s^{-1})
A1	$AE < 61$	$AE* < 163$	$Kp < 1.33$	$V_{sw} < 389.5$	$V_{sw}B_z > 282$
A2	$61 \leq AE < 125$	$163 \leq AE* < 314$	$1.33 \leq Kp < 2$	$389.5 \leq V_{sw} < 440$	$282 \geq V_{sw}B_z > -263$
A3	$125 \leq AE < 279$	$314 \leq AE* < 573$	$2 \leq Kp < 3$	$440 \leq V_{sw} < 522.4$	$-263 \geq V_{sw}B_z > -1018$
A4	$279 \leq AE < 606$	$573 \leq AE* < 1036$	$3 \leq Kp < 4.33$	$522.4 \leq V_{sw} < 643.1$	$-1018 \geq V_{sw}B_z > -2535$
A5	$606 \leq AE < 811$	$1036 \leq AE* < 1323$	$4.33 \leq Kp < 5.33$	$643.1 \leq V_{sw} < 698$	$-2535 \geq V_{sw}B_z > -3679$
A6	$AE \geq 811$	$AE* \geq 1323$	$Kp \geq 5.33$	$V_{sw} \geq 698$	$V_{sw}B_z \leq -3679$

3. Magnetic Local Time Variation of Electron Flux

To form a statistical average of the global distribution of the electron population, measurements of the electron flux from each of the POES satellites were collated and binned by both MLT and L^*. Physically, the L^* parameter is another form of the third adiabatic invariant, Φ, [*Roederer*, 1970] and is given by

$$L^* = \frac{-2\pi k_0}{\Phi R_E} \quad (1)$$

where R_E is the radius of the Earth and k_0 is the Earth's dipole moment. L^* was calculated with the UNILIB software library using the International Geomagnetic Reference Field and the Tsyganenko 96 (T96) model [*Tsyganenko*, 1995]. T96 was chosen as this model has an explicitly defined realistic magnetopause and does not uniquely apply to storm times. There was enough data on the solar wind and geomagnetic indices to apply the model to the whole data set. Each MLT bin covered 1 h, centered on the hour, and L^* spanned from 1 to 8, divided into 28 groups of width $L^* = 0.25$. To investigate the evolution of the electron flux distribution with changing activity, the flux data were further sorted into the six activity levels, defined by either AE, AE^*, Kp, V_{sw}, or $V_{sw}B_z$ listed in Table 1. These levels have been determined by the percentiles stated in section 2.2. By using AE, AE^*, Kp, V_{sw}, and $V_{sw}B_z$ to individually bin the flux readings, a more complete picture of the changes to the global distribution with increasing activity can be obtained.

Figure 3 shows the mean of each L^*-MLT bin, spatially arranged to give the average electron flux distribution for each of the six activity levels defined by AE. Each row corresponds to >30, >100, or >300 keV electrons, and the mini dial beneath each map displays the number of values sampled at each MLT and L^* location. In some regions, no electron flux data outside of the drift and bounce loss cones can be obtained from either telescope of the MEPED instrument. One such region forms a clear ring of missing data between $L^* = 1.5-2$, separating the region where T0 measures trapped flux from the region where T90 measures trapped flux. Excluding isolated regions, there are generally ~10,000 values at each L^*-MLT location, giving a good statistical significance to the average. At the lower activities considered, this can be much higher, potentially up to ~100,000 readings. Averages calculated from 10 or fewer flux measurements were not shown in Figure 3.

Figures 3a–3f shows that, with increasing activity, the flux level rises significantly, particularly for the >30 keV electron flux. At this energy the flux increase is mostly localized to the dawnside of the Earth, resulting in a notable MLT asymmetry in the electron flux distribution. This is consistent with electrons transported in from the plasma sheet drifting out of the magnetosphere on the dayside. For >100 keV electrons (Figures 3g–3l), as activity rises, the flux increase is again largest in the dawn sector. Even the >300 keV flux distributions (Figures 3m–3r) show a dawnside increase in electron flux that is moderately higher than on the duskside. At the lowest activity level (Figures 3a, 3g, and 3m), no notable MLT variation in the flux is seen for any of the electron energies studied, implying that 40% of the time (from Figure 2) no significant MLT variation is present throughout the radiation belt region at these energies. Although not shown here, similar plots of the electron flux distribution, ordered by AE^*, Kp, V_{sw}, and $V_{sw}B_z$, showed a comparable flux increase with rising activity level that was highest on the dawnside.

Two ring-like structures, separated by a region of lower flux, can be observed in the >30 keV and >100 keV global electron flux distributions shown in Figure 3. There is some suggestion of this structure at >300 keV, but this is less apparent as the majority of the inner zone flux at this energy seems to lie in the L^* range where neither T0 nor T90 observe electrons outside of the loss cone. With increasing AE, for >30, >100, and >300 keV electron flux, the inner edge of the outer ring moves earthward and the two belts become less defined. A model by *Liu et al.* [2003] has shown that electrons below 150 keV can be injected into $L^* = 3$ during times of high activity. *Thorne et al.* [2007] then showed that chorus waves could act to accelerate these "slot region" electrons to higher energies, resulting in slot region filling for electrons up to around 800 keV. Other processes such as radial diffusion may also be important for slot filling. A further study by *Reeves et al.* [2016] examining Van Allen Probes data concluded that slot region filling is common at energies below a few 100 keV. The reduction in the two-belt structure in the average flux distributions with increasing activity shown in Figure 3 supports this conclusion.

Statistical global electron flux distributions, similar to those in Figure 3, have been shown previously by *Thorne et al.* [2007] for 153 keV and 340 keV electrons measured by the Combined Release and Radiation Effects Satellite at three levels of AE^*. A notable difference to those presented here is the flux level of the inner belt. *Thorne et al.* [2007] showed that, at lower activities, the inner region contained the highest electron flux.
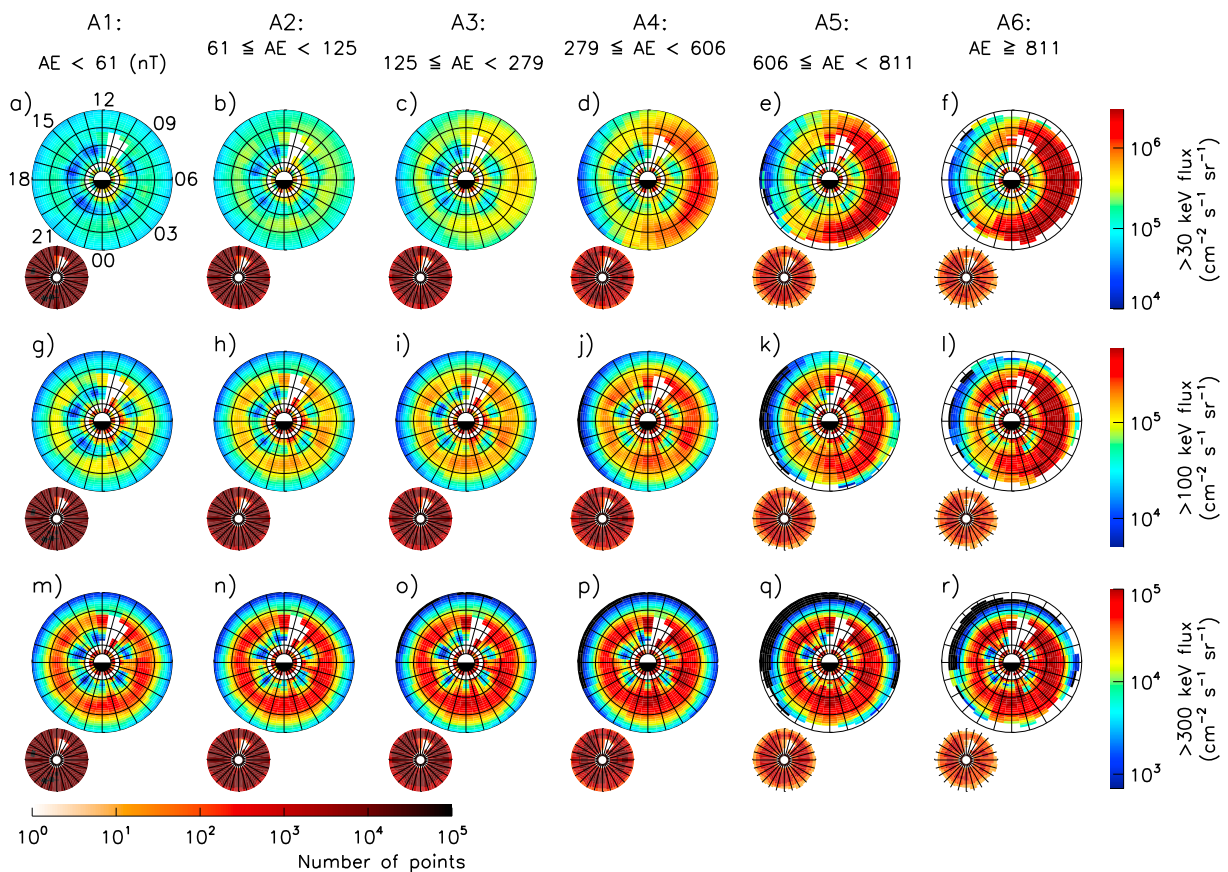
Figure 3. (a–r) Average flux distributions for >30 keV, >100 keV, and >300 keV electrons observed by the POES satellites over the stated date range, ordered by six *AE* levels. The plots are orientated in the equatorial plane with noon at the top and dawn to the right. The plots extend out to *L** = 8, and markers denote the *L** = 2, 4, and 6 positions.

This has been affirmed by *Reeves et al.* [2016] when considering the energy-dependent radial distribution of the radiation belts. However, in Figure 3 the flux of the inner region is comparable to that of the outer belt. The POES satellites generally observe flux with low equatorial pitch angles, approximately 11° at *L** ~ 3. Pitch angle distributions (PADs) in the inner belt exhibit large pitch angle anisotropies with a peak near 90°, while at larger *L** values, distributions are significantly flatter [*Shi et al.*, 2016]. The electron flux measurements presented by *Thorne et al.* [2007] and *Reeves et al.* [2016] are representative of large pitch angle electrons near 90°. Considering the anisotropic PADs in the inner belt, we would expect the electron flux measured by POES satellites to be somewhat smaller than the flux at large equatorial pitch angles presented by *Thorne et al.* [2007] and *Reeves et al.* [2016]. Further out, as the PADs tend to be considerably flatter, the difference between flux at high and low pitch angles might not be so large.

To quantify the extent of the variation of the electron flux in MLT at a particular *L** distance, flux measurements taken between 04 and 09 MLT (the dawn sector) were collated and a mean calculated. An average flux for the MLT range 16 to 21 (the dusk sector) was determined in the same manner. The ratio was then taken between these dawn and dusk averages, henceforth referred to as the dawn-dusk flux ratio. Three *L** bins were studied in this way, *L** = 4.125, 5.125, and 6.125, covering the outer radiation belt region. At each *L** value the dawn-dusk flux ratio was plotted against the activity level. This was repeated for each of the five activity metrics included in this study and is shown in Figure 4. It should be noted that *L** is dependent on the magnetic configuration, and it is possible that for very active periods *L** > 5 may not always exist. Here we simply present the dawn-dusk flux ratios according to POES satellite readings and *L** calculated using T96 as the external field model. Regardless of the activity metric used to define the activity levels, the ratios presented in Figure 4 are calculated from more than a thousand flux measurements.
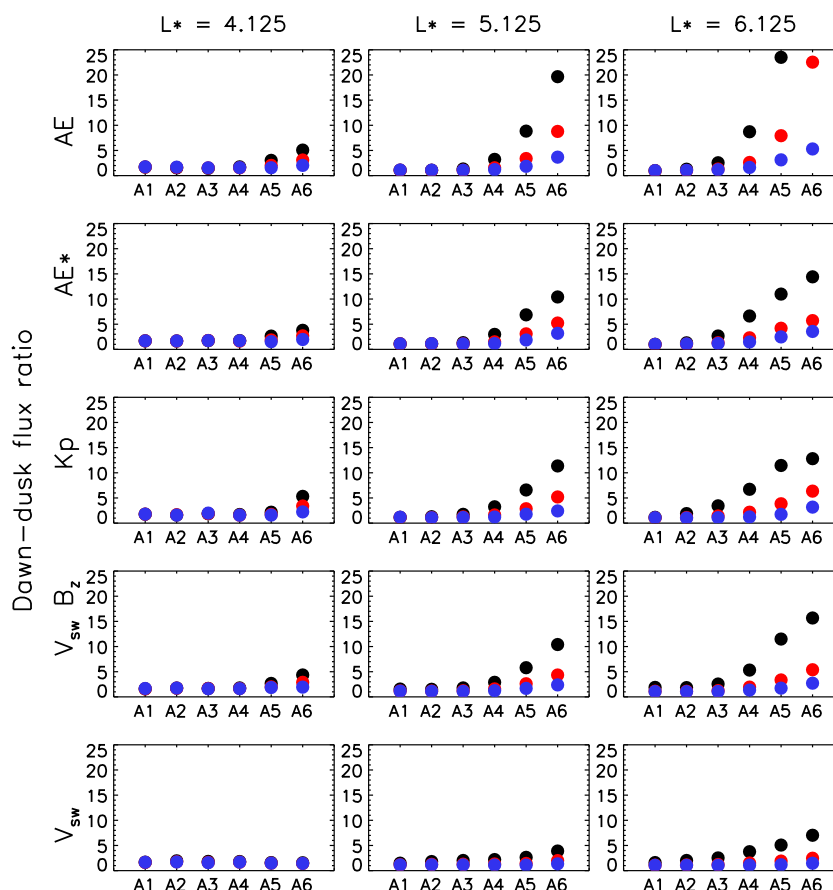
Figure 4. Ratio of the average electron flux in the dawn sector to average flux in the dusk sector at each activity level defined by AE, AE^*, Kp, $V_{sw}B_z$, and V_{sw} for three L^* values. Ratios for the >30 keV flux are in black, the >100 keV flux in red, and the >300 keV flux in blue.

It is apparent from Figure 4 that the dawn-dusk flux ratio can be much greater than 1 and can exceed a factor of 20. The largest dawn-dusk ratios are for the >30 flux (black circles), but the >100 keV and >300 keV flux ratios (red and blue circles) also suggest a dawn-dusk flux asymmetry with values which can be larger than 5. The dawn-dusk flux variation tends to increase with activity level for all five activity metrics. Additionally, for a given activity level, the ratios increase with L^*. Periods of high activity are generally associated with an enhanced convection electric field [*Kivelson*, 1976] and hence enhanced sunward electron motion. Additionally, at a fixed MLT and time, electrons drifting at a larger L^* will cross the equator farther from the Earth than those drifting at a smaller L^*. At a particular MLT, the equatorial magnetic field strength tends to be weaker the farther you are from the Earth. A weaker magnetic field results in a reduction in magnetic drifts and an increase in the convective drift velocity. Consequently, at the same MLT, electrons at larger L^* are potentially more likely to be on open drift paths due to the convection electric field than those at smaller L^*. What is perhaps surprising is that the dawn-dusk flux ratio for >300 keV electrons also rises with increasing activity and L^*. This is a much higher energy than that used as a low-energy boundary in most drift-averaged radiation belt models [e.g., *Glauert et al.*, 2014a; *Shprits et al.*, 2013; *Varotsou et al.*, 2008].

Dawn-dusk flux asymmetries were largest for A5 and A6 at $L^* = 6.125$ when activity levels were defined by AE. This is likely due to the AE index being related to substorm injections and not subjected to the same time blurring as AE^* (which is the highest level of AE over the previous 3 h). For a given level of activity, e.g., A5, the dawn-dusk flux ratios for AE^*, Kp, and $V_{sw}B_z$ are similar; however, the corresponding level for V_{sw} is consistently lower. At no V_{sw} defined activity level does any dawn-dusk ratio exceed 10. AE and AE^* are both direct measures of currents associated with substorms, and Kp is a direct measure of the magnetic field variation caused by a geomagnetic disturbance. The solar wind velocity is not a direct measure of geomagnetic activity, it is one factor along with the B_z component of the interplanetary magnetic field that drives substorms

and electron injections. During periods of fast solar wind and fluctuating interplanetary magnetic field, more energy is loaded into the system which then results in periods of overall enhanced convection and substorms. As a result, the combination of V_{sw} and B_z gives dawn-dusk flux ratios that are more consistent with AE, AE^*, and Kp. Kellerman and Shprits [2012] showed that tens of keV to MeV electron fluxes measured at geostationary orbit correlated well with V_{sw} once a suitable time delay had been applied. It is stressed that the observations presented here do not disagree with this. The flux in each of the three energy channels does increase with increasing V_{sw}, but this flux increase is more uniform in MLT.

Figure 4 shows a range of dawn-dusk ratios, extending from below 1 to more than 20. The question is then at what level does an MLT variation become problematic for models which use a drift-average approximation? As the low-energy flux is larger at dawn than the drift average, models applying an acceleration process to the average flux are likely to result in flux levels for higher-energy electrons that are lower than observed. We suggest that to obtain a result to a factor of 3 agreement with data, a dawn-dusk ratio exceeding 3 is significant. Regardless of the activity measure used to define the levels, below activity level A3, a dawn-dusk ratio exceeding 3 is not observed. This indicates that a minimum electron energy (E_{min}) of 30 keV would be valid in 3-D radiation belt models that do not extend beyond $L^* = 6.125$ provided that during the time frame considered AE, AE^*, Kp, and V_{sw} do not exceed 125 nT, 314 nT, 2, and 440 km s^{-1}, respectively, and $V_{sw}B_z$ is above -263 nT km s^{-1}. From Figure 2, this condition could be fulfilled 60% of the time. Radiation belt models are, however, mainly used to study periods of high activity to understand the physical processes involved [Glauert et al., 2014b; Li et al., 2014; Albert et al., 2009; Shprits et al., 2013]. Figure 4 shows that during the higher levels of activity defined by AE (A4, A5, and A6) the >30 keV dawn-dusk ratios can exceed 20 or, when activity is defined by AE^*, Kp, or V_{sw}, ratios can exceed an order of magnitude. In this case, a higher value of E_{min} could be required. While the dawn-dusk ratios for the >100 and >300 keV flux are lower than those for the >30 keV flux, ratios exceeding 3 are still observed at A5 and A6. The implication is that an E_{min} of 100 or 300 keV may only be suitable 95% or 98% of the time, respectively.

Figure 5a shows that the mean dawnside >30 keV flux increases with AE throughout the radiation belt region. The mean duskside >30 keV flux (Figure 5b) also increases comparably below $L^* \sim 4$ but, for $L^* \gtrsim 5$, the rise in the average duskside flux from activity levels A1 to A3 is less than on the dawnside. Beyond A3 the average duskside flux actually drops with increasing activity. For >100 keV electrons, the average dawnside flux (Figure 5c) again increases throughout the radiation belt region as the activity rises. However, the average duskside flux (Figure 5d) only increases with activity for $L^* \lesssim 5$. At larger L^*, the average duskside flux again falls with rising activity and the peak in the flux-L^* profile shifts from $L^* \sim 5$ to $L^* \sim 4$. This is a particularly interesting feature and is discussed further in the following section.

Perhaps, the most intriguing dawn-dusk average flux variation is that observed for the >300 keV electrons. At this energy the average dawnside flux (Figure 5e) rises with increasing activity for $L^* \lesssim 5.5$, and then remains approximately constant with increasing AE until $L^* \sim 6.2$, after which the flux begins to fall as activity increases. Conversely, the average duskside flux at >300 keV (Figure 5f) shows similar behavior to the duskside >30 keV and >100 keV flux (Figures 5b and 5d). For dusk sector MLTs, the average flux rises with activity out to $L^* \sim 4.5$ and then, at larger L^*, the average flux falls as activity increases. In the dusk sector, the peak in the flux-L^* profile moves from $L^* \sim 5$ to $L^* \sim 4$ with rising activity. As a result, the dawn-dusk ratios greater than 3 observed at $L^* = 6.125$ for the >300 keV electron flux in Figure 4 arise due to a duskside depletion rather than a dawnside enhancement.

As L^* is dependent on the magnetic field configuration it is possible that during some active periods not all L^* values in the $L^* = 3-8$ range may exist. Here we have presented the average dawnside and duskside flux-L^* profiles calculated using 14 years of POES electron flux measurements. Dawn or dusk flux averages that were calculated from fewer than 100 measurements were not plotted in Figure 5. While Figure 5 only shows the average dawnside and duskside flux-L^* profiles for the six activity levels defined by AE, the average dawnside and duskside flux distributions with changing AE^*, Kp, and $V_{sw}B_z$ showed similar trends. When activity was defined by V_{sw}, increasing V_{sw} did not result in a decrease in the average duskside flux for $L^* \gtrsim 5$ for >30, >100, or >300 keV electrons. The average dawnside and duskside flux both rose with V_{sw} for almost all L^*. As discussed previously, this is perhaps due to solar wind speed not being a direct measure of geomagnetic activity.
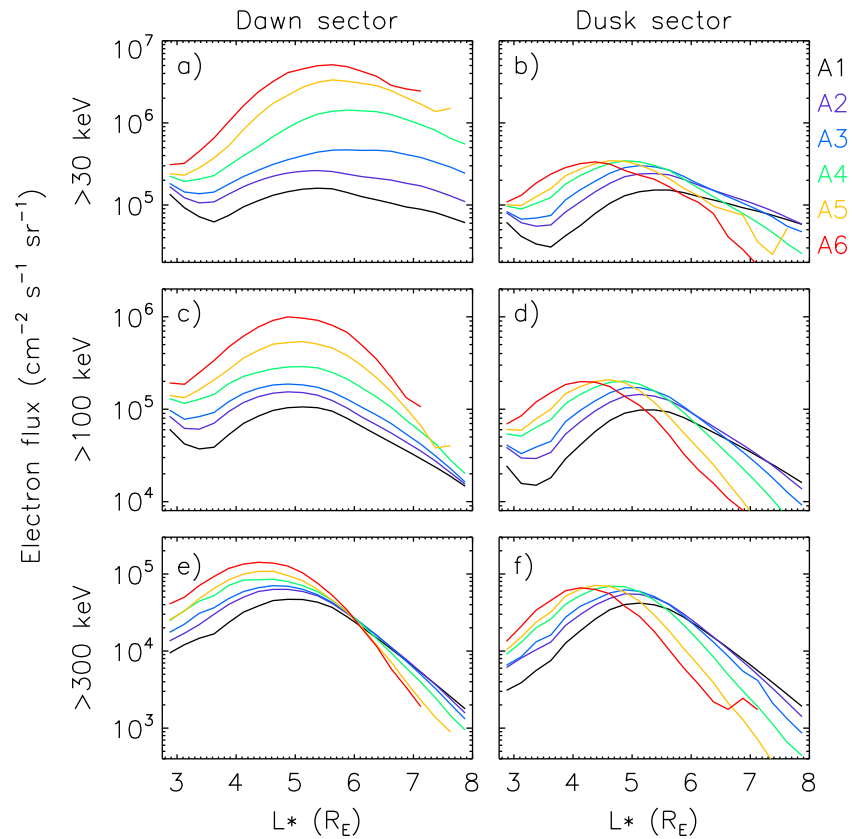
Figure 5. Average dawn sector and dusk sector electron flux-$L*$ profiles for >30, >100, >300 keV electrons. The profiles for each of the six activity levels defined by AE index are shown here, each in a different color.

4. Discussion

The trajectories of equatorially mirroring electrons, which have starting energies of 30, 100, and 300 keV on the dawnside of the Earth (at $X = 0$), are shown in Figure 6. Here we use a dipole magnetic field together with the Volland-Stern electric field [*Maynard and Chen*, 1975] assuming a constant $Kp = 5.33$ (Figure 6a), relating to the lower bound of the highest Kp activity level, and a constant $Kp = 7.00$ (Figure 6b). The drift paths are calculated for several starting radial distances between 4 and 7.5 R_E for each electron energy. POES satellites observe electrons with much lower pitch angle than 90° but, for the sake of simplicity, only the trajectories of equatorially mirroring electrons have been shown here. The observed dawn-dusk asymmetry for >30 keV electrons measured by the POES satellites occurs due to an increase in the dawnside flux throughout the outer radiation belt region that is not reflected on the duskside. On the duskside the average electron flux for $L* \gtrsim 5$ actually falls with rising activity. This is consistent with open drift paths causing electrons to leave the magnetosphere before reaching the dusk sector, resulting in a postsubstorm enhancement that is strongest in the dawn sector. Chorus waves are observed mainly on the dawnside of the Earth [*Meredith et al.*, 2012] and would act to precipitate electrons of a few tens of keV. However, since the >30 keV electron flux is higher at dawn than dusk, this suggests substorm injections are efficient at supplying electrons at low equatorial pitch angles, operating at a faster rate than electrons can be lost by chorus precipitation. Electrons >100 keV will also likely be injected into the region following substorms [*Cayton et al.*, 1989], causing an increase in the average dawnside flux. At this energy, the electrons could *also* be on open drift paths, which may help to cause the observed dawn-dusk flux asymmetry shown in section 3.

In Figures 6a and 6b, for both $Kp = 5.33$ and $Kp = 7.00$, respectively, the electrons that pass the dawnside with an energy of 300 keV at a distance between 4 and 7.5 R_E are not on open drift paths unlike some, or all, of the corresponding drifts for 30 and 100 keV electrons. However, the 300 keV electron trajectories have been perturbed by the convection electric field and, depending on the location of the magnetopause, this could still result in electrons encountering the magnetopause before completing a full drift. Inward motion
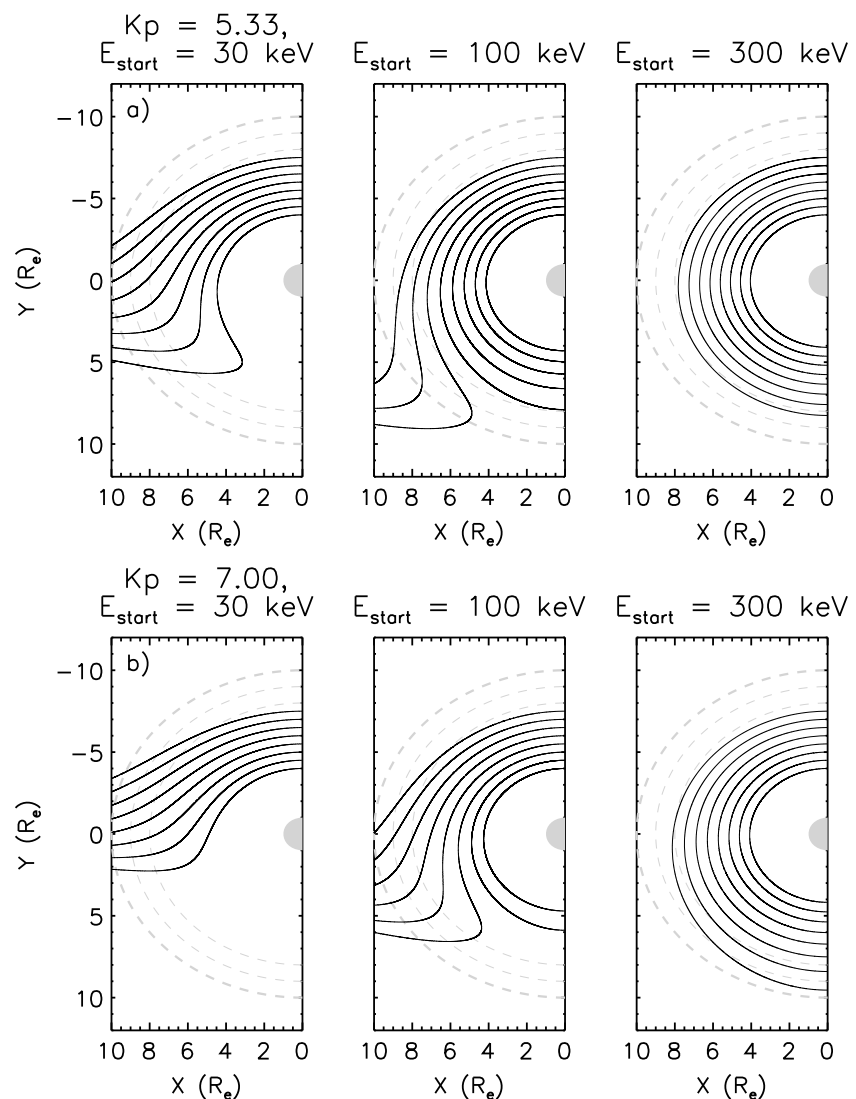
Figure 6. Drift paths of equatorially mirroring electrons in a dipole magnetic field for a Volland-Stern electric field assuming a constant Kp of (a) 5.33 and (b) 7.00. The drift paths shown start on the dawnside of the Earth at radial distances between 4 and 7.5 R_E and relate to electrons with starting energies of 30, 100, and 300 keV. The dashed lines mark radial distances of 8, 9, and 10 R_E for reference.

of the magnetopause to lower L shells in response to the increased solar wind pressure, or magnetic erosion of flux on the dayside through reconnection [*Herrera et al.*, 2016; *West et al.*, 1972], could ultimately prevent electrons at the larger L shells from traveling round the Earth to the dawnside of the planet. *Shprits et al.* [2006] showed that magnetopause shadowing may then drive further outward radial diffusion down to $L^* \sim 4$. Additionally, in a nondipole magnetic field, other factors such as the ∇B drift arising from a day-night gradient in the magnetic field [*Keika et al.*, 2005], caused by solar wind compression of the magnetosphere, may further alter drift paths, increasing the likelihood that electrons with an energy of 100 or 300 keV on the dawnside of the Earth will encounter the magnetopause before completing a full drift.

Aside from magnetopause shadowing, other processes, such as electron scattering due to wave-particle interactions, could cause a reduction in the duskside flux. On the duskside, loss processes such as interactions with hiss or electromagnetic ion cyclotron (EMIC) waves can scatter electrons into the loss cone, removing them from the region [*Meredith et al.*, 2004; *Kersten et al.*, 2014]. *Meredith et al.* [2004] showed that while equatorial hiss is not typically significant beyond a McIlwain L value of $L = 5$, midlatitude hiss is observed beyond $L = 6$ in the MLT range 12–15. EMIC waves have been shown to be strong where the ring current overlaps the plasmasphere [*Kersten et al.*, 2014] and act on electrons with pitch angles below $\sim$45° [*Usanova et al.*, 2014].

Due to the low-altitude polar orbit of the POES satellites, the pitch angles of the electron flux at $L^* = 5–6$ are comfortably below 45°. However, EMIC waves generally act on electrons of energies in excess of 500 keV [*Albert*, 2003; *Meredith et al.*, 2003; *Summers and Thorne*, 2003] so would likely only account for a small portion of the duskside loss. Furthermore, the reduction in the duskside flux is most pronounced during the highest level of activity, for which ∼99.995% of *AE* measurements greater than 811 nT are accompanied by the magnetopause moving below $L = 8$ in the preceding hour. The magnetopause location was calculated using the widely used Shue Model [*Shue et al.*, 1998] with the 1 R_E correction applied [*Case and Wild*, 2013]. It was therefore assumed that the largest contribution to the reduction in the average duskside electron flux during periods of high activity was magnetopause shadowing effects.

In Figure 5f a decrease in the average >300 keV duskside flux was observed with increasing activity beyond $L^* \sim 5$. Without a rapid supply of >300 keV electrons, a perturbed magnetopause is likely to cause a decrease in flux that rapidly affects all MLT, particularly at >300 keV. However, the average dawnside >300 keV flux (Figure 5e) does not show the same reduction and instead the average flux increases with activity until $L^* \sim 5$, and so alone magnetopause shadowing cannot explain the observed asymmetries in the >300 keV flux. A very similar result to Figure 5 was obtained when *AE** was used to define the activity levels (not shown). As *AE** is the highest value of *AE* in the preceeding 3 h, introduced by *Meredith et al.* [2004] to help account for electron drift time, this suggests variations between the dawnside and duskside flux-L^* profiles are not due to the transit time of electrons. Chorus wave acceleration may help to sustain the dawnside flux by acting on electrons of lower energy, accelerating them to 300 keV and beyond. However, the timescale for this acceleration is several hours or more, longer than the drift time of ∼300 keV electrons [*Horne et al.*, 2005].

Sergeev et al. [1992] suggest that an observed "drifting energetic electron hole" (a short, small decrease in the energetic electron flux) and the subsequent simultaneous enhancement of electron fluxes extending from 200 keV to ∼1 MeV during the 7 May 1986 may be a result of the dipolarization of field lines on the nightside. This is the reconfiguration of the magnetic field from stretched tail-like structure to a quasi-dipole-like formation [*Sauvaud and Winckler*, 1980; *Sugiura et al.*, 1968]. Electrons can then undergo nonadiabatic local acceleration as a result of the induced electric field associated with the magnetic fluctuations. Additionally, the changing magnetic field can cause alterations to the electron drift shells. It is possible that the average dawnside >300 keV flux rising or remaining mostly constant with activity as seen in Figure 5 is a result of this process. *Sergeev et al.* [2014] again showed observations of dispersionless injections at geostationary orbit across a range of energies extending from a few tens of keV to more than 350 keV shortly after a dipolarization onset, which includes the energy range of interest. Further work considering dipolarization fronts and associated changes in the O+ population has shown that nonadiabatic acceleration, likely due to dipolarization events, can occur in the inner magnetosphere at McIllwain $L < 6.6$ [*Nosé et al.*, 2016]. Similar enhancements have also been observed in the electron population at $L \sim 5.5$ up to MeV energies, again these have been linked to intense dipolarization electric fields [*Dai et al.*, 2015]. The variation between the average dawnside and duskside >300 keV flux seen at $L^* \leq 6$ may thus be in part due to this mechanism.

If an electron is unable to complete a drift around the Earth solely due to the geomagnetic field configuration, then the magnetic flux enclosed in the drift is infinite, hence we have an undefined L^* value. Considering this, in the Northern Hemisphere, for the ascending phase of the satellite orbit, the POES electron flux measurements for the 5° of magnetic latitude (Lat_{mag}) following the first undefined L^* value were binned by the magnetic latitude change (ΔLat_{mag}) and MLT. For the descending phase of the orbit, in this hemisphere, the electron flux measurements for the 5° of Lat_{mag} prior to the last undefined L^* value were binned by ΔLat_{mag}. The situation described above was reversed when the satellite was in the Southern Hemisphere. Calculating the mean of flux measurements in each MLT-ΔLat_{mag} bin gave the average electron flux distribution outside the last L^* value in terms of the magnetic latitude change. Figure 7 shows the result of this analysis for the six activity levels defined by *AE**. Using this activity metric should help mitigate the effect of the electron drift time from the average. The average flux for >30, >100, and >300 keV electrons on drift paths that will likely encounter the magnetopause rose with activity for dawnside MLTs (to the left of the dashed white line). Average electron flux increases with *AE** are not evident for many of the dusk sector MLT bins, and it would appear that the increase in electron flux occurs mostly for the midnight to dawn MLT range. It is likely that electrons encountering the magnetopause prevents the enhanced dawnside population from propagating to the dusk flank. That this trend is observed for >300 keV electrons as well as for >30 and >100 keV electrons is consistent with rapid enhancements of the >300 keV electron population supplying electrons to the dawnside of the Earth faster than they can be lost to the magnetosphere. The dawn sector flux enhancement at >300 keV
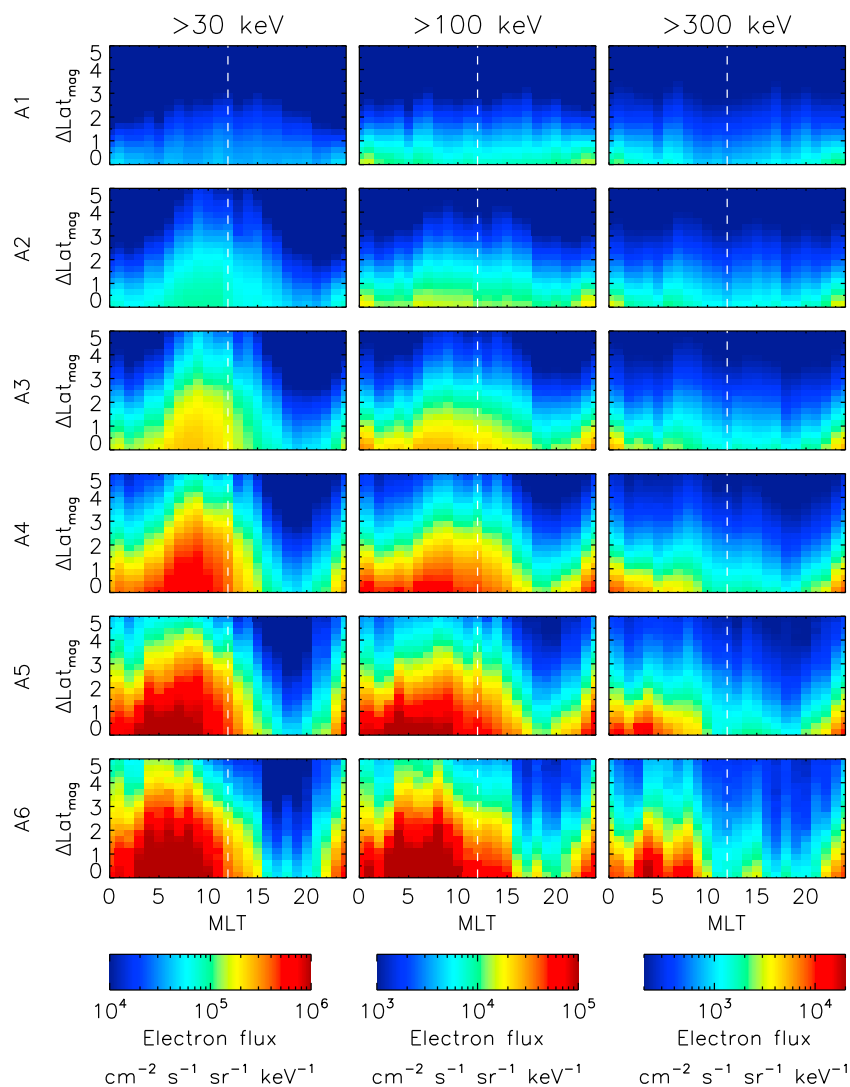
Figure 7. The >30, >100, and >300 keV electron flux measured by the POES satellites binned by *AE**, MLT, and the magnetic latitude change from the magnetic latitude of the last defined *L** value.

could therefore be an indication of electrons being injected with energies beyond 300 keV, potentially as a result of intense induced electric fields associated with some dipolarization events. For drift paths which encounter the magnetopause, this effect may result in dawn-dusk flux asymmetries, as observed in Figure 7.

Electrons with energies of hundreds of keV and above being injected into the radiation belt region as a result of intense dipolarization electric fields would provide a population of higher-energy electrons which could then be further accelerated by other processes such as wave-particle interactions and radial transport. In the absence of magnetopause shadowing and at lower *L** values, these electrons would likely be on closed drift paths and could then contribute to the relativistic electron population. Chorus waves acting on this population may help explain the rapid occurrence of MeV electrons sometimes observed during storm time [*Reeves et al.*, 1998; *Horne et al.*, 2005].

Aside from the mechanisms discussed, other factors could also result in dawn-dusk flux asymmetries. An enhanced convection electric field could perturb the drift orbits, not necessarily to open drift paths [*Kavanagh et al.*, 1968], but may result in electrons transiting the dusk sector at a larger *L** than in the dawn sector. By conservation of the first and second adiabatic invariants, outward motion to a larger *L** would cause a reduction in the electron energy, potentially to below the lower threshold of the energy channel. As discussed in section 2.1, the electron flux tends to fall with increasing energy [*Cayton et al.*, 1989; *Sergeev et al.*, 1992]. Therefore, electrons just above the lower threshold of the energy channel would be expected to constitute

a significant portion of the measured flux. If these electrons were to move outward and decrease in energy, a reduction in flux may be observed in the dusk sector compared to the flux at dawn.

The results presented in section 3 are based on measurements taken at low Earth orbit and, as a result, are representative of low equatorial pitch angles. It is noted that chorus waves propagating primarily in the dawn sector are likely to diffuse electrons to lower pitch angles, while on the duskside, chorus waves are less intense [*Horne et al.*, 2013]. However, the change in equatorial pitch angle distributions caused by wave-particle inter-actions typically occurs over many drift orbits [*Lyons et al.*, 1972], and as a result the pitch angle distributions on the dawnside are unlikely to be extensively different to those on the dusk. Recent findings by *Shi et al.* [2016] using Van Allen Probes data support this. They examined the anisotropy of electron pitch angle distri-butions for three levels of activity and found dawn-dusk variations in the anisotropic pitch angle distributions for 100, 200, and 350 keV electrons were not evident for any of the three activity levels.

The observation of a significant dawn-dusk flux ratio that increases with geomagnetic activity has impor-tant implications for modeling studies. Drift-average models set a lower energy boundary between 10 keV and ~200 keV. Our results support that the boundary should be set at higher energy with increasing activ-ity; otherwise, the models may underestimate or overestimate the acceleration and loss processes. However, the disadvantage of setting the boundary at a higher energy is that, since most models use a coordinate system based on the first invariant, it restricts simulations of the radiation belts at lower L^* to increasingly higher energies. Recent work has highlighted the importance of seed population acceleration in the genera-tion of relativistic and ultrarelativistic electrons [*Thorne et al.*, 2013] indicating that processes acting on lower energy electrons are crucial to understanding the radiation belt region as a whole. In order to include electrons of lower energy in radiation belt calculations, a convection-diffusion model is needed. An example of two convection-diffusion models are the Versatile Electron Radiation Belt-4D model [*Shprits et al.*, 2015] and the Asymmetric Physical Radiation Belts model [*Bourdarie et al.*, 1997]. The clear MLT dependence of the >30 keV and >100 keV electrons during active conditions highlights the importance of the development of these MLT-dependent models in order to better understand the region. Statistical studies such as that presented here could help provide boundary conditions for such models.

After an active period, the flux over an L shell will likely return to being mostly homogeneous in MLT. This is indicated by the electron flux for activity levels below A3 which did not show a notable MLT asymmetry. Dawn-dusk flux asymmetries set up during the period of high activity will likely degrade over several drift periods. Typically, 3-D radiation belt models use an activity time series to model changes to the electron population. We have shown that during periods of high activity, dawn-dusk flux asymmetries may occur in the electron flux distribution at the lower energies. Such flux asymmetries along an electron drift shell may cause inconsistencies between 3-D model results and data. We suggest here that one way to address such an issue and to improve 3-D radiation belt model results is by careful selection of the energy of the low-energy boundary.

5. Summary and Conclusions

A statistical study of the global distribution of the >30, >100, and >300 keV electron population has been presented using data spanning 14 years from the multisatellite low Earth orbit POES constellation. *AE*, *AE**, *Kp*, V_{sw}, and $V_{sw}B_z$ have each been used to define six activity levels to study the change in the global electron flux distribution with increasing activity. Our principle results are the following:

1. With increasing activity the average >30 keV electron flux increased. This rise in flux was primarily localized to the dawn sector, resulting in an MLT asymmetry in the electron flux distribution which can be more than a factor of 20. Asymmetrical >30 keV flux distributions may be due to electrons at this energy being on open drift paths following a substorm injection.
2. As the average >30 keV flux was seen to be higher in the dawn sector than the dusk during periods of high activity and remains so throughout the dawn sector, this suggests that electron injections are more efficient at supplying ~30 keV electrons than chorus precipitation is at removing them at the low pitch angles observed.
3. The average >100 keV flux for $L^* \lesssim 5$ rose with activity on both the dawnside and duskside of the Earth. For $L^* > 5$, the average dawnside flux continued to rise with activity while the average duskside flux decreased, resulting in flux asymmetries which can be of the order of a factor of 20 when *AE* was used to define activity.

4. As activity increases, the >300 keV average dawnside flux rose for $L^* \lesssim 6$. On the duskside, the peak of the average flux-L^* distribution shifts inward with rising activity and the flux increases for $L \lesssim 5$. Exterior to this L^* range, the flux decreases as activity rises. We suggest that the asymmetry observed in the >300 keV electron flux distribution is due to the combination of magnetopause shadowing, causing a duskside loss, and injections of >300 keV electrons, from some dipolarization fronts, sustaining the dawnside flux level.

5. Below activity level A3 (corresponding to $AE < 125$ nT, $AE^* < 314$ nT, $Kp < 2$, $V_{sw} < 440$ km s^{-1}), and $V_{sw}B_z > -263$ nT km s^{-1}), no dawn-dusk asymmetry in the flux distribution greater than a factor of 3 was observed. We therefore suggest that drift-averaged radiation belt models could set a minimum energy of 30 keV at $L^* \sim 6$ when modeling periods of low to moderate activity. For more active periods, a larger value of E_{min} is required; otherwise, the models may overestimate or underestimate the acceleration and loss processes. At activity level A3 and beyond, E_{min} should be larger than 100 keV and should be set to approximately 300 keV for very extreme activities.

In addition to being a useful indicator for the location of the minimum energy in 3-D radiation belt models, this study, together with the previous studies that considered lower energy electrons [e.g., *Li et al.*, 2014; *Bortnik et al.*, 2007], has also highlighted that, during times of high activity, measured electron fluxes at energies below ∼300 keV should only be considered representative of the MLT at which the values were recorded. Flux levels measured by low-energy instruments, such as the Helium, Oxygen, Proton, and Electron (HOPE) mass spectrometer and Magnetic Elec21ton Ion Spectrometer (MagEIS) on the Van Allen Probes, could vary depending on whether the spacecraft was on the duskside or dawnside of the Earth by more than an order of magnitude during geomagnetically active periods. This potential variation should be taken into account when analyzing low-energy electron flux data and highlights the importance of multiple satellites when investigating radiation belt electrons at energies below 300 keV.

References

Albert, J. M. (2003), Evaluation of quasi-linear diffusion coefficients for EMIC waves in a multispecies plasma, *J. Geophys. Res.*, *108*, 1249, doi:10.1029/2002JA009792.

Albert, J. M., N. P. Meredith, and R. B. Horne (2009), Three-dimensional diffusion simulation of outer radiation belt electrons during the 9 October 1990 magnetic storm, *J. Geophys. Res.*, *114*, A09214, doi:10.1029/2009JA014336.

Arnoldy, R. L., and K. W. Chan (1969), Particle substorms observed at the geostationary orbit, *J. Geophys. Res.*, *74*(21), 5019–5028, doi:10.1029/JA074i021p05019.

Birn, J., M. F. Thomsen, J. E. Borovsky, G. D. Reeves, D. J. McComas, R. D. Belian, and M. Hesse (1998), Substorm electron injections: Geosynchronous observations and test particle simulations, *J. Geophys. Res.*, *103*(A5), 9235–9248, doi:10.1029/97JA02635.

Bortnik, J., R. M. Thorne, and N. P. Meredith (2007), Modeling the propagation characteristics of chorus using CRRES suprathermal electron fluxes, *J. Geophys. Res.*, *112*, A08204, doi:10.1029/2006JA012237.

Bourdarie, S., D. Boscher, T. Beutier, J.-A. Sauvaud, and M. Blanc (1997), Electron and proton radiation belt dynamic simulations during storm periods: A new asymmetric convection-diffusion model, *J. Geophys. Res.*, *102*, 17,541–17,552, doi:10.1029/97JA01305.

Boyd, A. J., H. E. Spence, C.-L. Huang, G. D. Reeves, D. N. Baker, D. L. Turner, S. G. Claudepierre, J. F. Fennell, J. B. Blake, and Y. Y. Shprits (2016), Statistical properties of the radiation belt seed population, *J. Geophys. Res. Space Physics*, *121*, 7636–7646, doi:10.1002/2016JA022652.

Case, N. A., and J. A. Wild (2013), The location of the Earth's magnetopause: A comparison of modeled position and in situ cluster data, *J. Geophys. Res. Space Physics*, *118*, 6127–6135, doi:10.1002/jgra.50572.

Cayton, T. E., R. D. Belian, S. P. Gary, T. A. Fritz, and D. N. Baker (1989), Energetic electron components at geosynchronous orbit, *Geophys. Res. Lett.*, *16*(2), 147–150, doi:10.1029/GL016i002p00147.

Chen, M. W., and M. Schulz (2001), Simulations of storm time diffuse aurora with plasmasheet electrons in strong pitch angle diffusion, *J. Geophys. Res.*, *106*(A2), 1873–1886, doi:10.1029/2000JA000161.

Dai, L., et al. (2015), Near-Earth injection of MEV electrons associated with intense dipolarization electric fields: Van Allen Probes observations, *Geophys. Res. Lett.*, *42*, 6170–6179, doi:10.1002/2015GL064955.

Denton, M. H., and J. E. Borovsky (2012), Magnetosphere response to high-speed solar wind streams: A comparison of weak and strong driving and the importance of extended periods of fast solar wind, *J. Geophys. Res.*, *117*, A00L05, doi:10.1029/2011JA017124.

Evans, D. S., and M. S. Greer, (2004), Polar Orbiting Environmental Satellite Space Environment Monitor-2: Instrument descriptions and archive data documentation, NOAA Tech. Mem. 93, version 1.4, Space Weather Prediction Cent., Boulder, Colo.

Glauert, S. A., R. B. Horne, and N. P. Meredith (2014a), Three-dimensional electron radiation belt simulations using the BAS radiation belt model with new diffusion models for chorus, plasmaspheric hiss, and lightning-generated whistlers, *J. Geophys. Res. Space Physics*, *119*, 268–289, doi:10.1002/2013JA019281.

Glauert, S. A., R. B. Horne, and N. P. Meredith (2014b), Simulating the Earth's radiation belts: Internal acceleration and continuous losses to the magnetopause, *J. Geophys. Res. Space Physics*, *119*, 7444–7463, doi:10.1002/2014JA020092.

Hardy, D. A., M. S. Gussenhoven, and E. Holeman (1985), A statistical model of auroral electron precipitation, *J. Geophys. Res. Space Physics*, *90*, 4229–4248, doi:10.1029/JA090iA05p04229.

Herrera, D., V. F. Maget, and A. Sicard-Piet (2016), Characterizing magnetopause shadowing effects in the outer electron radiation belt during geomagnetic storms, *J. Geophys. Res. Space Physics*, *121*, 9517–9530, doi:10.1002/2016JA022825.

Horne, R. B., and R. M. Thorne (2003), Relativistic electron acceleration and precipitation during resonant interactions with whistler-mode chorus, *Geophys. Res. Lett.*, *30*(10), 1527, doi:10.1029/2003GL016973.

Horne, R. B., R. M. Thorne, S. A. Glauert, J. M. Albert, N. P. Meredith, and R. R. Anderson (2005), Timescale for radiation belt electron acceleration by whistler mode chorus waves, *J. Geophys. Res.*, *110*, A03225, doi:10.1029/2004JA010811.

Horne, R. B., R. M. Thorne, S. A. Glauert, N. P. Meredith, D. Pokhotelov, and O. Santolík (2007), Electron acceleration in the Van Allen radiation belts by fast magnetosonic waves, *Geophys. Res. Lett.*, *34*, L17107, doi:10.1029/2007GL030267.

Horne, R. B., T. Kersten, S. A. Glauert, N. P. Meredith, D. Boscher, A. Sicard-Piet, R. M. Thorne, and W. Li (2013), A new diffusion matrix for whistler mode chorus waves, *J. Geophys. Res. Space Physics*, *118*, 6302–6318, doi:10.1002/jgra.50594.

Jaynes, A. N., et al. (2015), Source and seed populations for relativistic electrons: Their roles in radiation belt changes, *J. Geophys. Res. Space Physics*, *120*, 7240–7254, doi:10.1002/2015JA021234.

Kavanagh, L. D., J. W. Freeman, and A. J. Chen (1968), Plasma flow in the magnetosphere, *J. Geophys. Res.*, *73*(17), 5511–5519, doi:10.1029/JA073i017p05511.

Keika, K., M. Nosé, S. Ohtani, K. Takahashi, S. P. Christon, and R. W. McEntire (2005), Outflow of energetic ions from the magnetosphere and its contribution to the decay of the storm time ring current, *J. Geophys. Res.*, *110*, A09210, doi:10.1029/2004JA010970.

Kellerman, A. C., and Y. Y. Shprits (2012), On the influence of solar wind conditions on the outer-electron radiation belt, *J. Geophys. Res.*, *117*, A05217, doi:10.1029/2011JA017253.

Kersten, T., R. B. Horne, S. A. Glauert, N. P. Meredith, B. J. Fraser, and R. S. Grew (2014), Electron losses from the radiation belts caused by EMIC waves, *J. Geophys. Res. Space Physics*, *119*, 8820–8837, doi:10.1002/2014JA020366.

Kim, K.-C., and Y. Shprits (2013), Long-term relativistic radiation belt electron responses to {GEM} magnetic storms, *J. Atmos. Sol. Terr. Phys.*, *100–101*, 59–67, doi:10.1016/j.jastp.2013.04.007.

Kivelson, M. G. (1976), Magnetospheric electric fields and their variation with geomagnetic activity, *Rev. Geophys.*, *14*(2), 189–197, doi:10.1029/RG014i002p00189.

Lam, M. M., R. B. Horne, N. P. Meredith, S. A. Glauert, T. Moffat-Griffin, and J. C. Green (2010), Origin of energetic electron precipitation >30 keV into the atmosphere, *J. Geophys. Res.*, *115*, A00F08, doi:10.1029/2009JA014619.

Li, W., R. M. Thorne, J. Bortnik, Y. Nishimura, V. Angelopoulos, L. Chen, J. P. McFadden, and J. W. Bonnell (2010), Global distributions of suprathermal electrons observed on THEMIS and potential mechanisms for access into the plasmasphere, *J. Geophys. Res.*, *115*, A00J10, doi:10.1029/2010JA015687.

Li, W., et al. (2014), Radiation belt electron acceleration by chorus waves during the 17 March 2013 storm, *J. Geophys. Res. Space Physics*, *119*, 4681–4693, doi:10.1002/2014JA019945.

Liu, S., M. W. Chen, L. R. Lyons, H. Korth, J. M. Albert, J. L. Roeder, P. C. Anderson, and M. F. Thomsen (2003), Contribution of convective transport to stormtime ring current electron injection, *J. Geophys. Res.*, *108*, 1372, doi:10.1029/2003JA010004.

Lyons, L. R., R. M. Thorne, and C. F. Kennel (1972), Pitch-angle diffusion of radiation belt electrons within the plasmasphere, *J. Geophys. Res.*, *77*(19), 3455–3474, doi:10.1029/JA077i019p03455.

Ma, Q., et al. (2015), Modeling inward diffusion and slow decay of energetic electrons in the Earth's outer radiation belt, *Geophys. Res. Lett.*, *42*, 987–995, doi:10.1002/2014GL062977.

Mann, I., T. O'Brien, and D. Milling (2004), Correlations between {ULF} wave power, solar wind speed, and relativistic electron flux in the magnetosphere: Solar cycle dependence, *J. Atmos. Sol. Terr. Phys.*, *66*(2), 187–198, doi:10.1016/j.jastp.2003.10.002.

Maynard, N. C., and A. J. Chen (1975), Isolated cold plasma regions: Observations and their relation to possible production mechanisms, *J. Geophys. Res.*, *80*(7), 1009–1013, doi:10.1029/JA080i007p01009.

Meredith, N. P., R. M. Thorne, R. B. Horne, D. Summers, B. J. Fraser, and R. R. Anderson (2003), Statistical analysis of relativistic electron energies for cyclotron resonance with EMIC waves observed on CRRES, *J. Geophys. Res.*, *108*, 1250, doi:10.1029/2002JA009700.

Meredith, N. P., R. B. Horne, R. M. Thorne, D. Summers, and R. R. Anderson (2004), Substorm dependence of plasmaspheric hiss, *J. Geophys. Res.*, *109*, A06209, doi:10.1029/2004JA010387.

Meredith, N. P., R. B. Horne, A. Sicard-Piet, D. Boscher, K. H. Yearby, W. Li, and R. M. Thorne (2012), Global model of lower band and upper band chorus from multiple satellite observations, *J. Geophys. Res.*, *117*, A10225, doi:10.1029/2012JA017978.

Meredith, N. P., R. B. Horne, J. D. Isles, and J. C. Green (2016), Extreme energetic electron fluxes in low Earth orbit: Analysis of POES e >30, e >100, and e >300 keV electrons, *Space Weather*, *14*, 136–150, doi:10.1002/2015SW001348.

Nosé, M., K. Keika, C. A. Kletzing, H. E. Spence, C. W. Smith, R. J. MacDowall, G. D. Reeves, B. A. Larsen, and D. G. Mitchell (2016), Van Allen Probes observations of magnetic field dipolarization and its associated O+ flux variations in the inner magnetosphere at L < 6.6, *J. Geophys. Res. Space Physics*, *121*, 7572–7589, doi:10.1002/2016JA022549.

O'Brien, T. P., R. L. McPherron, D. Sornette, G. D. Reeves, R. Friedel, and H. J. Singer (2001), Which magnetic storms produce relativistic electrons at geosynchronous orbit?, *J. Geophys. Res.*, *106*(A8), 15,533–15,544, doi:10.1029/2001JA000052.

Reeves, G. D., D. N. Baker, R. D. Belian, J. B. Blake, T. E. Cayton, J. F. Fennell, R. H. W. Friedel, M. M. Meier, R. S. Selesnick, and H. E. Spence (1998), The global response of relativistic radiation belt electrons to the January 1997 magnetic cloud, *Geophys. Res. Lett.*, *25*(17), 3265–3268, doi:10.1029/98GL02509.

Reeves, G. D., et al. (2013), Electron acceleration in the heart of the Van Allen radiation belts, *Science*, *341*(6149), 991–994, doi:10.1126/science.1237743.

Reeves, G. D., et al. (2016), Energy-dependent dynamics of keV to meV electrons in the inner zone, outer zone, and slot regions, *J. Geophys. Res. Space Physics*, *121*, 397–412, doi:10.1002/2015JA021569.

Rodger, C. J., B. R. Carson, S. A. Cummer, R. J. Gamble, M. A. Clilverd, J. C. Green, J.-A. Sauvaud, M. Parrot, and J.-J. Berthelier (2010a), Contrasting the efficiency of radiation belt losses caused by ducted and nonducted whistler-mode waves from ground-based transmitters, *J. Geophys. Res.*, *115*, A12208, doi:10.1029/2010JA015880.

Rodger, C. J., M. A. Clilverd, J. C. Green, and M. M. Lam (2010b), Use of POES SEM-2 observations to examine radiation belt dynamics and energetic electron precipitation into the atmosphere, *J. Geophys. Res.*, *115*, A04202, doi:10.1029/2008JA014023.

Roederer, J. (1970), *Dynamics of Geomagnetically Trapped Radiation*, Physics and chemistry in space, vol. 2, Springer, Berlin.

Sauvaud, J.-A., and J. Winckler (1980), Dynamics of plasma, energetic particles, and fields near synchronous orbit in the nighttime sector during magnetospheric substorms, *J. Geophys. Res.*, *85*(A5), 2043–2056, doi:10.1029/JA085iA05p02043.

Sergeev, V. A., T. Bösinger, R. D. Belian, G. D. Reeves, and T. E. Cayton (1992), Drifting holes in the energetic electron flux at geosynchronous orbit following substorm onset, *J. Geophys. Res.*, *97*(A5), 6541–6548, doi:10.1029/92JA00182.

Sergeev, V. A., et al. (2014), Event study combining magnetospheric and ionospheric perspectives of the substorm current wedge modeling, *J. Geophys. Res. Space Physics*, *119*, 9714–9728, doi:10.1002/2014JA020522.

Shi, R., D. Summers, B. Ni, J. F. Fennell, J. B. Blake, H. E. Spence, and G. D. Reeves (2016), Survey of radiation belt energetic electron pitch angle distributions based on the Van Allen Probes MagEIS measurements, *J. Geophys. Res. Space Physics*, *121*, 1078–1090, doi:10.1002/2015JA021724.

Shprits, Y., D. Subbotin, B. Ni, R. Horne, D. Baker, and P. Cruce (2011), Profound change of the near-Earth radiation environment caused by solar superstorms, *Space Weather*, *9*(8), S08007, doi:10.1029/2011SW000662.

Shprits, Y. Y., R. M. Thorne, R. Friedel, G. D. Reeves, J. Fennell, D. N. Baker, and S. G. Kanekal (2006), Outward radial diffusion driven by losses at magnetopause, *J. Geophys. Res.*, *111*, A11214, doi:10.1029/2006JA011657.

Shprits, Y. Y., D. Subbotin, A. Drozdov, M. E. Usanova, A. Kellerman, K. Orlova, D. N. Baker, D. L. Turner, and K.-C. Kim (2013), Unusual stable trapping of the ultrarelativistic electrons in the Van Allen radiation belts, *Nat. Phys.*, *9*, 699–703, doi:10.1038/nphys2760.

Shprits, Y. Y., A. C. Kellerman, A. Y. Drozdov, H. E. Spence, G. D. Reeves, and D. N. Baker (2015), Combined convective and diffusive simulations: VERB-4D comparison with 17 March 2013 Van Allen probes observations, *Geophys. Res. Lett.*, *42*, 9600–9608, doi:10.1002/2015GL065230.

Shue, J.-H., et al. (1998), Magnetopause location under extreme solar wind conditions, *J. Geophys. Res.*, *103*(A8), 17,691–17,700, doi:10.1029/98JA01103.

Sigsbee, K., J. D. Menietti, O. Santolík, and J. S. Pickett (2010), Locations of chorus emissions observed by the polar plasma wave instrument, *J. Geophys. Res.*, *115*, A00F12, doi:10.1029/2009JA014579.

Subbotin, D. A., and Y. Y. Shprits (2009), Three-dimensional modeling of the radiation belts using the Versatile Electron Radiation Belt (VERB) code, *Space Weather*, *7*(10), S10001, doi:10.1029/2008SW000452.

Sugiura, M., T. L. Skillman, B. G. Ledley, and J. P. Heppner (1968), Propagation of the sudden commencement of July 8, 1966, to the magnetotail, *J. Geophys. Res.*, *73*(21), 6699–6709, doi:10.1029/JA073i021p06699.

Summers, D., and R. M. Thorne (2003), Relativistic electron pitch-angle scattering by electromagnetic ion cyclotron waves during geomagnetic storms, *J. Geophys. Res.*, *108*, 1143, doi:10.1029/2002JA009489.

Thorne, R. M. (2010), Radiation belt dynamics: The importance of wave-particle interactions, *Geophys. Res. Lett.*, *37*(22), L22107, doi:10.1029/2010GL044990.

Thorne, R. M., Y. Y. Shprits, N. P. Meredith, R. B. Horne, W. Li, and L. R. Lyons (2007), Refilling of the slot region between the inner and outer electron radiation belts during geomagnetic storms, *J. Geophys. Res.*, *112*, A06203, doi:10.1029/2006JA012176.

Thorne, R. M., et al. (2013), Rapid local acceleration of relativistic radiation-belt electrons by magnetospheric chorus, *Nature*, *504*, 411–414, doi:10.1038/nature12889.

Tsyganenko, N. A. (1995), Modeling the Earth's magnetospheric magnetic field confined within a realistic magnetopause, *J. Geophys. Res.*, *100*(A4), 5599–5612, doi:10.1029/94JA03193.

Tu, W., G. S. Cunningham, Y. Chen, S. K. Morley, G. D. Reeves, J. B. Blake, D. N. Baker, and H. Spence (2014), Event-specific chorus wave and electron seed population models in DREAM3D using the Van Allen Probes, *Geophys. Res. Lett.*, *41*, 1359–1366, doi:10.1002/2013GL058819.

Usanova, M. E., et al. (2014), Effect of EMIC waves on relativistic and ultrarelativistic electron populations: Ground-based and Van Allen Probes observations, *Geophys. Res. Lett.*, *41*, 1375–1381, doi:10.1002/2013GL059024.

Varotsou, A., D. Boscher, S. Bourdarie, R. B. Horne, S. A. Glauert, and N. P. Meredith (2005), Simulation of the outer radiation belt electrons near geosynchronous orbit including both radial diffusion and resonant interaction with whistler-mode chorus waves, *Geophys. Res. Lett.*, *32*, L19106, doi:10.1029/2005GL023282.

Varotsou, A., D. Boscher, S. Bourdarie, R. B. Horne, N. P. Meredith, S. A. Glauert, and R. H. Friedel (2008), Three-dimensional test simulations of the outer radiation belt electron dynamics including electron-chorus resonant interactions, *J. Geophys. Res.*, *113*, A12212, doi:10.1029/2007JA012862.

West, H. I., R. M. Buck, and J. R. Walton (1972), Shadowing of electron azimuthal-drift motions near the noon magnetopause, *Nat. Phys. Sci.*, *240*, 6–7, doi:10.1038/physci240006a0.